Mechanistic description of Lead sorption onto nanoplastics

Florent Blancho, Mélanie Davranche, Adrien Leon, Rémi Marsac, Stephanie Reynaud, Bruno Grassl, Julien Gigault

View Article Online
View Journal

Environmental Science Nano

Accepted Manuscript

This article can be cited before page numbers have been issued, to do this please use: F. Blancho, M. Davranche, A. Leon, R. Marsac, S. Reynaud, B. Grassl and J. Gigault, *Environ. Sci.: Nano*, 2024, DOI: 10.1039/D3EN00677H.

ROYAL SOCIETY OF CHEMISTRY

rsc.li/es-nano

View Article Online
DOI: 10.1039/D3EN00677H

Environmenta Significance Statement:

The findings presented in this study shed light on several crucial aspects of nanoplastics that underscore their environmental significance. Nanoplastics exhibit a remarkably high surface reactivity with respect to adsorption. This heightened reactivity implies that they can readily interact with various environmental constituents, potentially affecting ecosystems and organisms. Furthermore, the study highlights the distinct metal adsorption capacities between nanoplastics and polymer nanobeads, underlining the importance of understanding the unique characteristics of different nanoplastic materials, such as size and shape, in the context of metal pollution. Additionally, the formation of mono and bi-ligand complexes with lead (Pb) and nanoplastics bearing -COOH groups elucidates the intricate chemical interactions occurring at the nanoplastic-water interface, emphasizing their potential role as carriers or modifiers of metal pollutants in aquatic systems.

View Article Online
DOI: 10.1039/D3EN00677H

Mechanistic description of Lead sorption onto nanoplastics

Florent Blancho[1], Mélanie Davranche[1], Adrien Léon[1], Rémi Marsac[1], Stéphanie Reynauld[2], Bruno Grassl[2], and Julien Gigault[3]

[1] Univ Rennes, CNRS, Géosciences Rennes – UMR 6118, F-35000 Rennes, France.

[2] IPREM, CNRS / Université de Pau et des Pays de L'Adour, F64000 Pau, France

[3] TAKUVIK laboratoy, UMI3376 CNRS / Université Laval, Québec, Canada

Abstract

Although it is currently recognized that nanoplastics (NPs) are present in the environment, their ability to carry metals or other contaminants and the processes involved are still poorly investigated. Yet, one of the significant threats of plastic debris is found in these associated species. The lack of relevant data is directly explained by our inability to collect enough nanoplastics from the environment for experimental investigation. The environmental NPs models that we have recently proposed offer new opportunities to characterize their interactions with metals. We have developed an adsorption model based on lead (Pb^{2+}) adsorption experiments (adsorption isotherm at pH 5.5 for Pb(II)/NPs ratios between 0.5 and 100 mg gC^{-1} and a pH adsorption edge between pH 2 and 8 for Pb(II)/NPs at 2.5 and 25 mg gC^{-1} relative to the studied NPs, Ionic strength = 5 mmol L^{-1} of $NaNO_3$) using various NPs models to describe surface complexation processes and to predict the sorption capacity of NPs. Model hypotheses have suggested that Pb is adsorbed onto NPs via carboxylic sites mainly as mono-ligand and bi-ligand complexes. The empirical model and linear free energy relationship validated the extrapolated stability constants and binding hypothesis. The adsorption capacities of nanoplastics are highly dependent on their surface oxidation state, shape heterogeneity

and aggregation which control their carboxylic site density, distribution and then availability. This metal-NPs affinity suggests that NPs could act as vectors of metals relative to their behavior regarding other natural adsorbent phases.

Keywords: Nanoplastics, Metals, Surface, Adsorption, Modeling

Introduction

Plastic pollution is one of the significant challenges of the Anthropocene Epoch. Plastics benefit society in innumerable ways, and their production has increased considerably over the last century. This results in the significant generation of plastic debris all throughout the world. Within the size continuum of plastic debris, it is now admitted that nanoscale plastics, i.e. nanoplastics (NPs), are present in our various environments [1–3]. Nanoplastics are colloidal particles < 1000 nm presenting a Brownian motion in aqueous systems, with open and heterogeneous shapes and non-homogeneous charged surfaces [4,5]. Due to these colloidal properties, nanoplastics are therefore potentially highly reactive, especially with regards to their surrounding dissolved contaminants, and they raise several urgent questions about their potential impact on these associated species.

As demonstrated for microplastics (MPs) by Brennecke et al. (2016a), Cu and Zn released from antifouling paint were adsorbed by polystyrene (PS) pellets and in higher concentrations by polyvinyl chloride (PVC) pellets [7]. Turner and Holmes (2015) demonstrated that MPs' metals adsorption is driven by the pH and that altered polymer pellets collected on beaches have a higher metal affinity than virgin pellets [8]. They explained these results as being due to the alteration of the surface that produced the functional sites as well as the presence of organic materials. Tang et al. (2021) used nylon MPs collected in the environment to show that Ni, Cu and Zn adsorption onto MPs is controlled by surface complexation and intraparticle diffusion processes. They also highlighted the importance of the O-containing group in metal adsorption. Recently, artificial neural network calculations have suggested that aged MPs have a higher affinity for metals than virgin MPs and that the sorption

capacity depends on the initial metal concentrations [10]. Nonetheless, considering the estimation by Besseling et al. (2019) that nanoparticles (i.e., those with sizes below 100nm in this context) could have concentrations 10^{14} times greater than microplastics, it follows that nanoparticles, due to their heightened surface area specificity, are expected to play a more significant influence on the speciation, transportation, and impact of metals within diverse environmental ecosystems.[4,12].

It is well accepted that the interaction between metals and plastic debris, from microplastics to nanoplastics, is a crucial process in their (eco)toxicological risk assessment. When NPs interact with a metal, this could also increase their bioavailability. During the bio-assimilation of NPs, the associated micropollutants could be released and accumulated in living organisms under favorable physicochemical conditions [13,14]. However, the mechanisms that control the interaction of NPs with metals are still unknown. This is partly explained by the need (and difficulty) to collect a significant amount of NPs from the environment for experimental investigation. To meet this challenge, several authors have produced NPs models. Three production methodologies are proposed:

i. Controlled emulsion-polymerization of spherical nanoparticles with or without a functionalized surface [15,16]

ii. Mechanical degradation of pristine polymer pellets, resulting in NPs with heterogeneous shapes and functional surface sites [17,18]

iii. Mechanical abrasion of highly altered plastics debris sampled in the environment, resulting in NPs with heterogeneous shapes and functional surface sites [19].

Although spherical nanoparticles are useful for instrumental calibration due to their controlled size, shape, composition and binding site density [15,16], these models are not environmentally relevant in terms of shape and size polydispersity [4]. NPs produced by mechanical degradation (polymer pellets and altered plastics debris) are polydisperse in size with heterogeneous and open shapes, as observed for environmental NPs [5,18,19]. However, there are essential differences between NPs produced from polymer pellets and plastic debris since they are not submitted to extreme surface photooxidation in the environment, which strongly influences their site density and, therefore, their reactivity. A first

study suggested that environmentally relevant models can bind metal (Pb) via surface complexation and intraparticle diffusion [12]. The experimental datasets demonstrated that e-NPs have a high binding affinity and capacity for Pb without clearly determining the mechanisms due to the lack of particle characterization.

Nevertheless, using rare earth elements as a mechanism probe [20], we demonstrated that Rare Earth Elements are bound to NPs (polystyrene latex or environmentally relevant NPs models) via surface carboxylic sites. For environmentally relevant NPs models, these –COOH sites are induced by natural weathering. Our recent study[20] suggested that trivalent metals formed mono and multidentate complexes with the –COOH sites of various NPs models as a function of the Rare Earth Elements concentration. The sorption mechanism is not yet identified and quantified. However, a surface complexation model could help to obtain this information. Although Rare Earth Elements (REE) are a reliable chemical probe, it is challenging to develop a model for each of the whole REE group. For this reason, we chose here to work with only Pb. Catrouillet et al.[21] showed that the presence of Pb localized on the altered surface layers of microplastics is attributed to its use as an additive during plastic manufacturing rather than originating from the environment. Lead (Pb) was one of the most commonly used metallic additives in plastic formulations.

This work aims to characterize and quantify the adsorption mechanisms between lead (Pb) and various NPs models: carboxylated polystyrene Latex nanoparticles ($PSL_{surfactant}$), soap-free carboxylated polystyrene Latex (PSL_{free})[15], polymorph and polysized nanoparticles (m-NPs)[22], and plastic nanoparticles produced from the altered layer of plastics debris collected in the environment (e-NPs)[19]. To achieve this, we generated experimental datasets through adsorption experiments conducted under various physicochemical conditions such as concentration and pH. These datasets were employed to assess different binding scenarios and to extrapolate sorption parameters. The model's validity was subsequently confirmed by comparing its predictions with experimental datasets found in the literature. In this context, geochemical modeling serves as a predictive tool for estimating speciation and testing mechanistic hypotheses.

View Article Online
DOI: 10.1039/D3EN00677H

Materials and methods

Chemicals and nanoplastics

All used chemicals were of analytical grade. The solutions were prepared with ultrapure water 108 (Milli-Q system, Millipore). The containers used were (i) trace-metal cleaned with 10% (v/v) HNO3 for 24 h at 45°C, (ii) soaked in and then rinsed with ultrapure water for 24 h at 45°C, and (iii) finally dried at 30°C. All solutions were prepared with ultrapure water (18.2 Ω, MilliQ, Millipore). The different nanoplastics (NPs) models used in the study are:

i. Commercial carboxylated polystyrene latex nanoparticles measuring 200 nm in size and conditioned with the surfactant (from Polysciences©, Germany) (i.e. $PSL_{surfactant}$);

ii. Soap-free (i.e. without surfactant) carboxylated polystyrene latex nanoparticles measuring 380 nm in size[15], (i.e. $PSL_{free,}$);

iii. polymorph and polysized nanoparticles produced from the milling of polystyrene pellets[18], (i.e. m-NPs);

iv. plastic nanoparticles produced from the altered layer of plastic debris collected in the environment[19] (i.e. e-NPs).

Nanoparticle Properties

The hydrodynamic diameter (D_h) of the NPs was determined using Dynamic Light Scattering (DLS) (VASCO Flex, Cordouan Technologies) for suspensions at 10 ppm without Ionic Strength (IS) (Fig. 1). The shape of the NPs was examined using transmission electronic microscopy (TEM) (JEM 2100 HR, Jeol). Transmission electronic microscopy was operated at an acceleration voltage of 200-kV with LaB_6 as an electron source, the point and line resolution were 2.3 Å and 1.4 Å, respectively. Particles were photographed with a Gatan Orius SC200D camera, and elemental analysis was performed using an EDX Oxford X-Max 80T detector. The TEM observations showed anisotropic e-

View Article Online
DOI: 10.1039/D3EN00677H

and m-NPs (Fig. 1C), in agreement with the previous studies [19,22]. The specific surface area (SSA) of the NPs was determined using the BET method using a Gemini VII instrument (Micromeritics) and according the ISO 9277-2022 protocol[23]. For the polystyrene latex particles, the specific surface area was extrapolated from the particle diameter and assuming that the surface is perfectly smooth. Their diameters were estimated through TEM images treated with ImageJ (n=50).

The surface charge was assessed by potentiometric titration using a Titrano unit controlled by the Tiamo software (Metrohm). All solutions were titrated with 0.01 M NaOH (Honeywell Fluka) under a N_2 flux. Before titration, the pH probe was calibrated on a concentration scale using 1mM HNO_3. Titrations were performed at 10, 100, and 1000 mM of $NaNO_3$ and were started below a pH of 4 by adding a fixed volume of 100 mM HNO_3. The determination of the protonable groups was performed as described by Spadini at al. (2018) (SI 2). The surface charge of the NPs was determined by performing a calculation using PHREEQC implemented by the SIT thermodynamic database (SI 2). Potentiometric titrations were used to determine the amount of ionizable function relative to the pH on the PSL surface (SI 2).

Adsorption experiments

Adsorption isotherms were carried out for the Pb(II)/NPs ratios between 0.5 and 100 mg gC^{-1}. The concentration of the NPs was fixed at 50 and 25 mg L^{-1} for the PSLs, e-NPs, and m-NPs, respectively. Note that the concentration of the NPs is in gC L^{-1}. The mass concentration was preferred over the particle number as it can be directly measured. The ionic strength (IS) was fixed with 5 mmol L^{-1} of $NaNO_3$. For adsorption isotherms, once Pb(II) was introduced into the NP suspensions, the pH was initially set and then continuously maintained at a pH of 5.5 ± 0.05. The filter cut-off used was 0.2 µm (filter syringe, PES, Sartorius) for the PSLs and 30 kDa (ultrafiltration device, PES, Sartorius) for the e-NPs and m-NPs. After filtration, all samples were acidified with 2% HNO_3 for the ICPMS analysis. The pH-adsorption edge experiments were performed with Pb(II)/NPs ratios of 2.5 and 25 mg gC^{-1} for the PSLs, e-NPs, and m-NPs, respectively. The pH range was investigated from 2 to 7 using HNO_3 or NaOH and the same method described for the isotherm adsorption. The targeted pH

were 2, 3, 4, 4.5, 5, 5.5, 6 and 7. Prior the Pb(II) adsorption on the nanoplastics, the saturation indices (SI) of Pb-based solid phases were calculated for experimental conditions of isotherm and the pH adsorption edge. The calculations were performed using PhreeQC and MINTEQA2 database, excluding any adsorption on NPs but including an equilibrium with the CO_2 from the atmosphere. The calculated SI, presented in the Fig. S3, are < 0 for all Pb-based solid phases reported. These results suggest no Pb-based solid precipitation for all condition studied. All adsorption experiments were performed in replicates (n=3).

Chemical Analysis

The lead concentrations were measured with a Quadrupole ICP-MS (Agilent Technologies 7700X). Before quantification of the metals, calibration curves were performed and validated using certified material references (SLRS-6, National Research Council). A rhodium solution was used as an internal standard to correct the instrumental drift and potential matrix effects. The limit of Pb quantification was determined at 0.0038 µg L^{-1}. Moreover, the samples were diluted if necessary as the upper limit of the Pb(II) calibration curve was 5 µg L^{-1}. The NPs concentrations were monitored with the carbon concentration using a Total Organic Carbon (TOC) analyzer (TOC-V Shimadzu).

Modeling approach

The study carried out by Blancho et al.[20] used two complementary modeling approaches. These authors demonstrated that REE binding onto PSLs and e-NPs is provided by REE adsorption onto -–COOH surface functions developed at the surface of the NPs. They also demonstrated that REE binding occurs through the formation of mono-ligand and multi-ligand complexes related to the surface properties of the NPs. Therefore, we tested these hypotheses using empirical models to evidence the formation of one or two complexes. The hypothesis of the formation of a single surface complex was tested by using a classical Langmuir isotherm model (Eq. 1), while the formation of weak (monoligand complex, Eq. 2) and strong (multi-ligand complex, Eq. 2) surface complexes was tested by using a double-Langmuir isotherm model. The potentially involved mechanisms were tested

and parameterized by accounting for electrostatic effects at the water interface of the NPs using a diffuse layer model (DLM). For both models, the modeling was based on the extrapolations of the experimental datasets, and a least-square fit determined all parameters.

The classical Langmuir model considers the possibility of forming one complex with the discrete surface sites of the adsorbent following the equation:

$$[Pb]_{ads} = Q_{max,\,Pb}\frac{K_{ads}[Pb]_{aq}}{1 + K_{ads}[Pb]_{aq}} \qquad \text{(Eq. 1)}$$

Where Q_{max} is the maximum amount of adsorbed Pb (µg g^{-1}), and K_{ads} is the Langmuir adsorption constant, $[Pb]_{ads}$ is the equilibrium adsorbed-phase concentration of Pb (µg g^{-1}), and $[Pb]_{aq}$ is the equilibrium aqueous-phase concentration of Pb in solution (µg g^{-1}).

The double Langmuir model considers the possibility of forming weak and robust complexes with the discrete surface sites of the adsorbent following the equation:

$$[Pb]_{ads} = Q_{weak\ max,\,Pb}\frac{K_{weak}[Pb]_{aq}}{1 + K_{weak}\,[Pb]_{aq}} + Q_{strong\ max,\,Pb}\frac{K_{strong}[Pb]_{aq}}{1 + K_{strong}\,[Pb]_{aq}} \qquad \text{(Eq. 2)}$$

where $Q_{weak/strong\ max,\,Pb}$ is the maximum amount of adsorbed Pb (µg g^{-1}) occurring as weak and robust complexes, and $K_{weak/strong}$ is the Langmuir adsorption constant for weak and strong complexes, respectively.

The mechanistic modeling (DLM) was performed using a combination of geochemical (PHREEQC version 2) and extrapolation (PhreePlot) programs (Parkhurst and Appelo 1999, Kinniburgh and Cooper 2011). PhreePlot was designed to fit experimental datasets while automatically using the speciation program PHREEQC. All of the datasets, i.e. the isotherm and the pH-adsorption edge of each nanoparticle, were used simultaneously for the fitting. The binding parameters are optimized by a modified Marquardt-Levenberg procedure [27]. The Pb(II) adsorption onto the NPs models was restricted to ionic Pb^{2+} as the dominant species in the studied pH range (SI 3). Blancho et al.[20] demonstrated that trivalent cations form mono-ligand (weak) and multi-ligand complexes (strong) with –COOH on the surface of the NPs. For this reason, the Pb sorption was modeled under two scenarios based on different sorption hypotheses. The first scenario explains the sorption of Pb by the

mono-ligand complex only (Eq. 3) and the second by the mono-ligand and bi-ligand complexes (Eq. 3 and 5). Here, the bi-ligand complex formation was chosen to represent the multi-ligand complex, i.e. strong binding. The best scenario was selected based on the RMSE values.

$$\text{NPs}\text{–}COO^- + {Pb_s}^{2+} \Leftrightarrow \text{NPs}\text{–}COOPb^+ \text{ (Eq. 3)} \quad \text{with} \quad K_{COOPb^+} = \frac{[NPs\text{–}COO^-] * [{Pb_s}^{2+}]}{[NPs\text{–}COOPb^+]} \qquad \text{(Eq. 4)}$$

$$2\ \text{NPs}\text{–}COO^- + {Pb_s}^{2+} \Leftrightarrow (NPs\text{–}COOH)_2Pb, \text{ (Eq. 5)} \qquad \text{with } K_{COO_2Pb} = \frac{[(Nps\text{–}COO^-)^2] * [{Pb_s}^{2+}]}{[NPs\text{–}COO_2Pb]} \text{ (Eq. 6)}$$

Results and Discussion

Nanoplastic characterization: Size and surface properties

The Fig. 1 presents the e-NPs and m-NPs size from characterization. For both nanoplastics, their log-transformed autocorrelation function (log-ACF) were inferior to the CRM 900 nm log-ACF, indicating that particles composing the NPs are inferior to 900 nm (blue and red line, Fig. 1A).

When compared to the certified reference materials (CRMs), both the log-ACF of e-NPS and m-NPs exhibited non-linearity (Fig. 1A), indicating the presence of polydispersed suspensions, a characteristic that is further confirmed by the relative polydispersity index (Table 1). The hydrodynamic diameter of e-NPs and m-NPs was estimated to 262 and 352 nm, respectively.

For the PSLs, as expected, the DLS results indicated a monodisperse suspension (i.e. straight Log-transformed ACF and a PDI ≈ 0.05 ± 0.01) (Fig. S1 and Table 1). The hydrodynamic diameter of $PSL_{surfactant}$ and PSL_{free} was estimated to 240 nm and 396 nm, respectively.

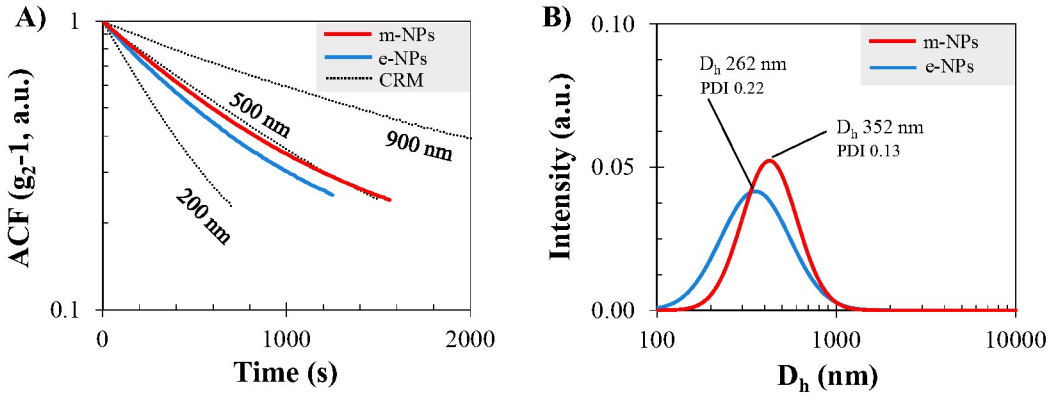

View Article Online
DOI: 10.1039/D3EN00677H

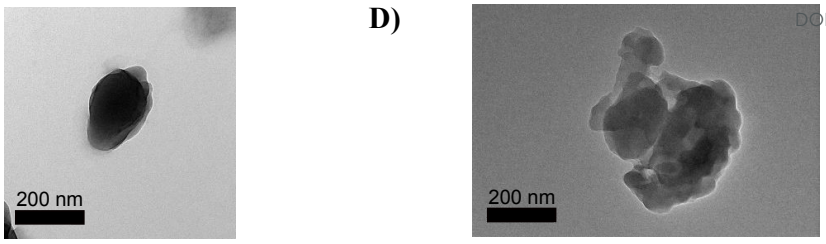

Fig. 1. NP size characterization. A) Log-transformed ACF of the e-NPs and m-NPs superimposed on CMRs standards (200, 500 and 900 nm). **B)** Population size distribution by intensity estimated with an ACF cumulant fit. **C-D)** TEM pictures of the e-NPs and m-NPs, respectively.

The Fig. 2 presents the proton interaction with the surface of the studied NPs, highlighting of proton reactive sites. As expected, the dissociation of such groups increased with increasing pH. The IS increasing also favored the surface group deprotonation by inducing an increase in the surface potential (Ψ_0) [28]. Titrations of both PSLs at 1M IS showed a typical sigmoidal curve [29,30]. These titration curves indicated that almost all the ionizable groups were dissociated between pH 4 and 8. The total surface ionizable group, Hs_{tot}, was considered equal to the concentration of the deprotonated group at pH 8. For the $PSL_{surfactant}$ and PSL_{free}, the Hs_{tot} was thus determined to $0.316 \pm 2\ 10^{-3}$ and $0.086 \pm 2\ 10^{-3}$ mmol g^{-1}, respectively. According to the SSA, the site density is equal to 6.60 and 3.41 sites nm^{-2} for $PSL_{surfactant}$ and PSL_{free}, respectively.

Table 1. Nanoplastic characteristics. Nanoplastic size and surface properties.

NPs	D_h (nm)	PDI	SSA ($m^2\ g^{-1}$)	Hs_{tot} (mmol g^{-1})	Site density (site nm^{-2})	pKa **	RMSE ***
$PSL_{surfactant}$	240	0.06	30.4*	$0.316 \pm 2e^{-3}$	6.60	**4.64 ± 0.01**	$3.2e^{-5}$
PSL_{free}	396	0.06	16.0*	$0.086 \pm 2e^{-3}$	3.41	**4.11 ± 0.02**	$1.7e^{-5}$
e-NPs	262	0.22	13.9	$\geq 0.282 \pm 4e^{-4}$	≥ 13.6	*4.76**	-
m-NPs	352	0.13	28.9	$\geq 0.037 \pm 1e^{-4}$	≥ 1.19	*4.76**	-

* SSA calculated from the particle size determined via TEM pictures (see Fig. S1 for the diameter size).

** pKa fixed to the acetate pKa (Martell and Smith 1977).

*** RMSE based on the pKa extrapolation.

The extrapolation of Hs datasets allowed us to calculate the intrinsic pKa of PSLs (Table 1, for further information please report to the SI 1). The $PSL_{surfactant}$ pKa was estimated to 4.64 which is a coherent value compare to known COOH pKa [31]. The PSL_{free} pKa was estimated to 4.11, which consistent with acid's pKa, used during its polymerization, estimated to 4.05 [32]. These results are also consistent with the pKa values determined for the carboxylic functional groups of natural organic matter [33].

View Article Online
DOI: 10.1039/D4EN00677H

Compare to PSLs, the e-NPs and m-NPs 1M titration curves were not sigmoidals (Fig. 2). An important Hs increased was observed after pH 7.5-8, avoiding any pKa extrapolation (Fig. 2). At pH 8.5, Hs_{tot} reached highest values, with $0.282 \pm 4\ 10^{-4}$ and $0.037 \pm 1\ 10^{-4}$ mmol g^{-1}, for the e-NPs and m-NPs, respectively. This late H^+ released may be induced by particle aggregates, known to delay the proton dissociation[34]. Prior titrations, strong aggregation was observed for both e-NPs and m-NPs, which wasn't observed for PSLs. The high particle concentration (≥ 5 g L^{-1}) and low pH (< 4) favored such aggregation. In front of this bottleneck, the e-NPs and m-NPs pKa were fixed to 4.76, the acid acetic pKa's value [31].

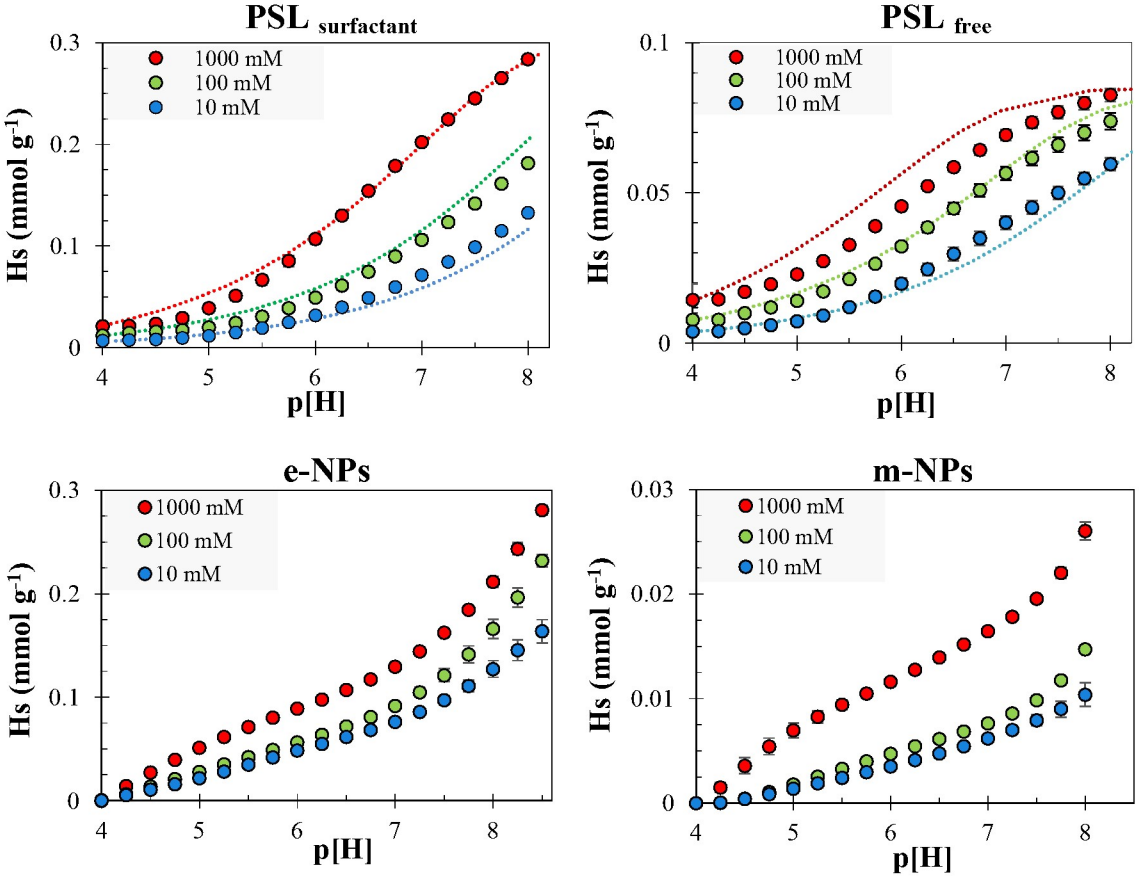

Fig. 2. Nanoplastic surface deprotonation. Nanoplastic surface group dissociation function of pH at 3 ionic strength (10, 100 and 1000 mM). The symbols correspond to the experimental data and the dotted lines to the calculated data.

Pb(II) adsorption by nanoplastics

The experimental and calculated Pb(II) adsorption isotherms and pH-adsorption edge are plotted in Fig. 3. The adsorption isotherms were concave, suggesting a progressive saturation of the binding

sites (Fig. 3). However, no plateau was reached, suggesting that site saturation was not reached or that adsorption was controlled by a multilayer or heterogeneous process. Significant adsorption capacity variations were obtained between the PSLs. For $[Pb]_{free}$ = 2ppm, $[Pb]_{ads}$ was 13 and 15 mg $g^{-1}C$ for $PSL_{surfactant}$ and PSL_{free}, respectively. This difference was consistent with the –COOH site density (Table 1). For the PSLs, the Pb(II) adsorption increased with the pH. Less than 5% of $[Pb]_{tot}$ was adsorbed at pH ≤ 4 versus 85% at pH ≥ 7 (Fig. 2). For the e-NPs and m-NPs, at $[Pb]_{free}$ = 0.4 ppm, $[Pb]_{ads}$ was ≈ 7.5 and 2.25 mg $g^{-1}C$, respectively (Fig. 3). These adsorbed concentrations were consistent with the total ionizable site density, Hs_{tot} (Table 1). The adsorption was also strongly dependent on the pH. Less than 15% of $[Pb]_{tot}$ was adsorbed for pH ≤ 4 versus 90% at pH 7. The pH-dependence of the adsorbed concentration highlights the competition between H^+ and Pb(II) for their adsorption onto the surfaces of the nanoparticles (Fig. 4)

View Article Online
DOI: 10.1039/D3EN00677H

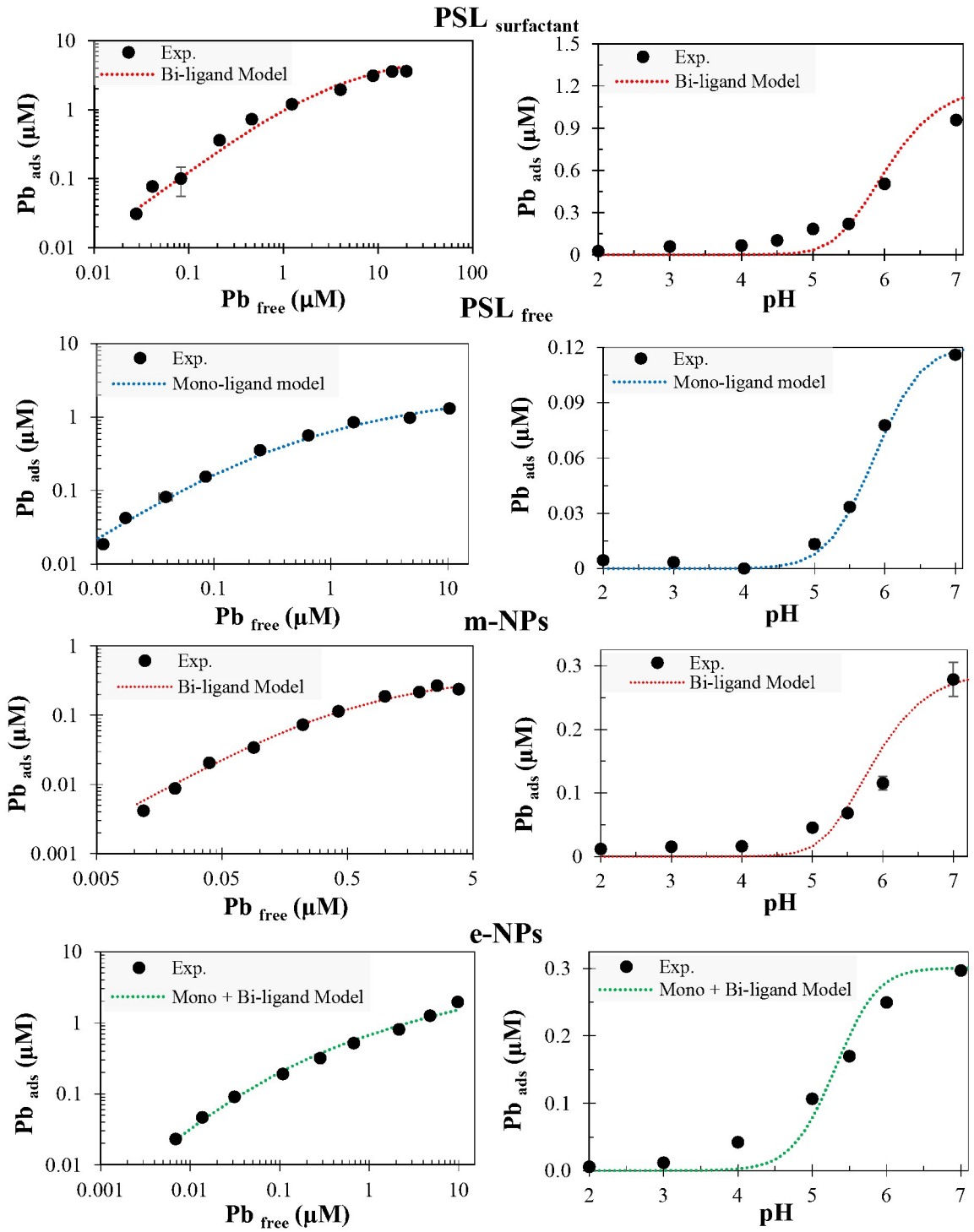

Fig. 3. Mechanical description of NP-Pb(II) adsorption datasets. Left, adsorption isotherms and right, pH adsorption edges. Dotted curves correspond to modeled datasets with a surface complexation model, including mono-ligand (blue), bi-ligand (red) or both (green) as possible complexes formed between Pb(II) and NP surface site.

View Article Online
DOI: 10.1039/D3EN00677H

Pb(II) adsorption modeling

The classical Langmuir model satisfactorily reproduced the experimental isotherm datasets for both PSLs and the m-NPs (Fig. 4, Table 2) with $Q_{max}(PSL_{surfactant}) > Q_{max}(PSL_{free}) > Q_{max}$(m-NPs) in agreement with their site density (Table 1). This result indicates a homogeneous adsorption process through only one complex formation. By contrast, the Log K increased from m-NPs to $PSL_{surfactant}$, indicating that surface complex formation was facilitated for the highest site density, i.e. for $PSL_{surfactant}$.

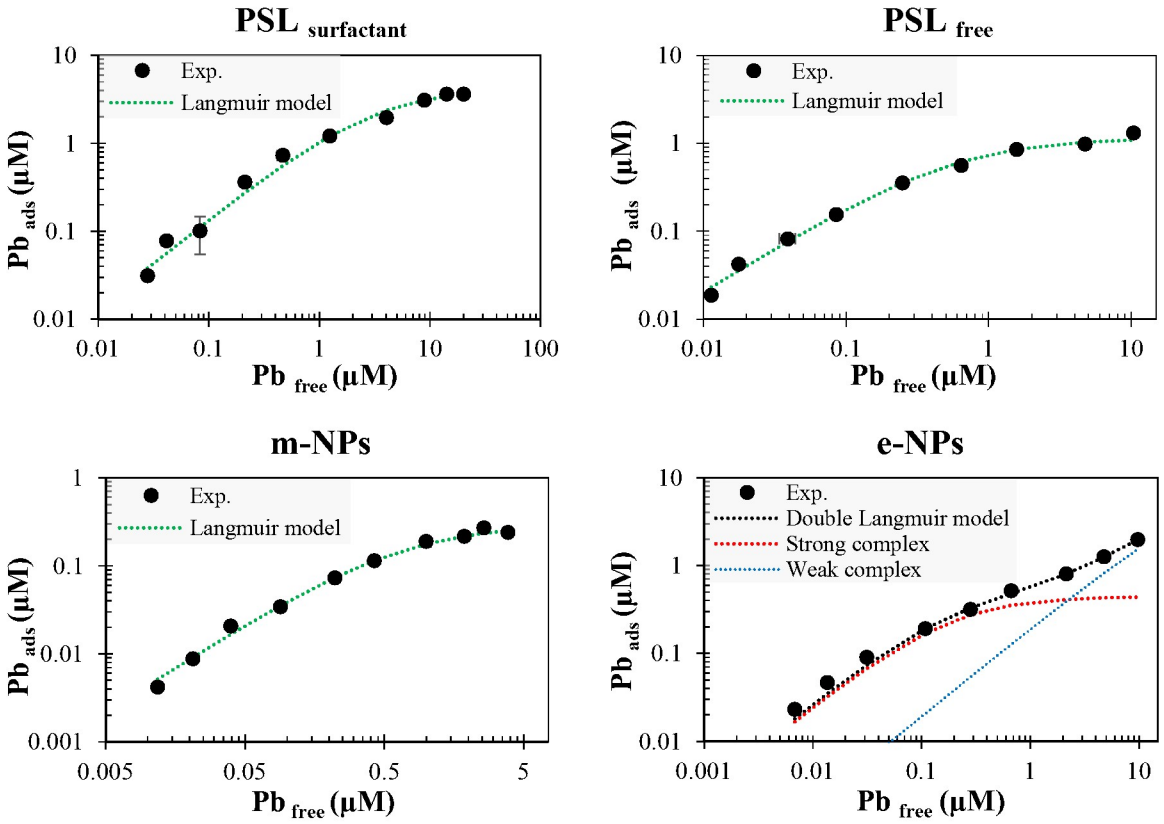

Fig. 4. Empirical description of NP Pb(II) isotherms. Isotherm datasets fitted with a Langmuir model for both PSLs and the m-NPs, and a double Langmuir model for the e-NPs.

For the e-NPs, the double Langmuir model reproduced the experimental isotherm datasets better (RMSE = 0.0007 versus 0.04 for the classical and double-Langmuir models, respectively (SI 4, Fig. S4). These results confirm a Pb(II) heterogeneous adsorption model onto the e-NPs, corresponding to the formation of at least two complexes. The complex formed at low Pb_{free} concentrations is dominant with Qmax = 7.5 µmol L^{-1} versus 0.45 µmol L^{-1} for the second complex

(red dotted curve). The formation of both complexes was in line with the e-NPs site density, which was the highest among the studied NPs (Table 1).

Table 2. Complexation parameters obtained with empirical and mechanistic approaches.

Langmuir parameters	**PSL $_{surfactant}$**	**PSL $_{free}$**	**m-NPs**	**e-NPs**
Q (µmol L^{-1}/ mmol g^{-1})	4.15 / 0.16	1.15 / 0.04	0.3 / 0.01	
log K	-0.5	0.3	1.8	
$RMSE_{langmuir}$	0.08	0.02	0.0005	
Q_{weak} (µmol L^{-1}/ mmol g^{-1})				7.06 / 0.27
log K_{weak}				-1.6
Q_{strong} (µmol L^{-1}/ mmol g^{-1})				0.408 /0.016
log K_{strong}				0.8
$RMSE_{double-Langmuir}$				0.0009
Surface complexation models	**PSL $_{surfactant}$ Bi-ligand**	**PSL free Mono-ligand**	**m-NPs Bi-ligand**	**e-NPs Mono- and Bi-ligand**
H_{stot} (mmol g^{-1})	0.32[a]	0.09[a]	0.037[a]	0.282[a]
$Hs_{bi-ligand}$ (mmol g^{-1})	-	-		0.02 [d]
SSA (m^2 g^{-1})	30.4[a]	16.0[a]	28.9[a]	13.9[a]
pKa	4.64[b]	4.11[b]	4.76[b]	4.76 [b]
Log $K_{mono\ (Weak)}$	-	2.3 ± 0.21[c]	-	2.72[c]
Log $K_{bi\ (Strong)}$	3.76[c]	-	4.94 ± 0.06[c]	=2*log K_{mono}
RMSE	0.203	0.03	0.019	0.107

a: fixed from analytical data (Table 1)
b: fixed and determined from potentiometric titrations (Table 1)
c: fitted from the mechanistic model
d: fixed to the strong complex density determined with the double-Langmuir model

With regards to the results obtained from the empirical models and the binding hypothesis suggested by Blancho et al. (2022), a one-complex model (homogeneous adsorption process) was tested for both PSLs and the m-NPs; a two-complex (weak mono-ligand and strong bi-ligand complexes, heterogeneous adsorption process) model was tested for the e-NPs. Following Blancho et al.[20], the –COOH functional groups were considered to be the only ones able to bind Pb onto the NPs.

Two hypotheses were tested for the one-complex model: the formation of mono-ligand complexes and the formation of bi-ligand models for both PSLs and the m-NPs. The best-fitting model (lowest RMSE) was reported in Fig. 5, except for the m-NPs, for which the model providing the more consistent log K value was retained (SI 5, Fig. S5). A comparison of both mono- and bi-ligand models for both PSLs and the m-NPs can be found in SI 5 and Fig. S5. Table 2 summarizes the fixed and fitted (calculated) binding parameters.

For e-NPs, only the mono + bi-ligand model was tested with regards to the double- Langmuir model result and the previous results of Blancho et al. [20], who suggested the formation of mono and multi-

ligand complexes between the e-NPs and REE. However, with this model, several assumptions had to be made to allow the model to converge (too many parameters to adjust). Therefore, the bi-ligand complex concentration was fixed equal to that determined by the double-Langmuir model, the log $K_{e\text{-}NPsCOOPb+}$ mono-ligand complex was fixed equal to the log $K_{CH3COOPb+}$ complex (2.38, Smith and Martell, 1989) and the bi-ligand complex log $K_{e\text{-}NPs(COO)2Pb}$ was fixed equal to 2*log K mono.

Mechanistic calculations demonstrated that Pb(II) was bound as a bi-ligand complex and a mono-ligand complex onto $PSL_{surfactant}$ and PSL_{free}, respectively (Fig. 3 and Table 2). These binding hypotheses are in agreement with their site density (Table 1), the Langmuir model calculations, and the previous results[20] obtained for REE. For $PSL_{surfactant}$, the calculated log $K_{(NPs\text{-}COO)2Pb}$ was 3.76, which was close to the log $K_{(CH3\text{-}COO)2Pb} = 4.08$ [31]. For PSL_{free}, the calculated log $K_{NPsCOOPb+}$ was 2.3, in line with the log $K_{CH3COOPb^+} = 2.68$ [31]. For the m-NPs, Pb(II) was bound as a bi-ligand complex, with log $K_{(CH3COO)2Pb} = 4.94$. This value is higher than that of $(CH_3COO)_2Pb$ with log K = 4.08, suggesting a high affinity for Pb. However, this affinity does not seem to agree with the m-NPs site density, which was the lowest among the studied m-NP_S (Table 1).

Nevertheless, although the site density is an important controlling parameter, the geometric distribution of the functional groups on the NPs surface can also influence the formed complex. Among all the studied NPs, m-NPs have the most heterogeneous shape (Fig. 1). Their size was also larger than that of the e-NPs suggesting the highest aggregation of the m-NPs (Table 1 and Fig. 1). Furthermore, the presence of -COOH functional groups can also be identified within the plastic crackles, potentially leading to a higher local site density. All these factors influence the geometrical distribution of the surface functional group and can explain that the –COOH sites are close enough to favor the formation of the bi-ligand complex with Pb. e-NPs formed mono and bi-ligand complexes with Pb(II), which was in agreement with the Langmuir calculations and binding hypothesis suggested by Blancho et al.[20] for REE, i.e. adsorption onto –COOH surface functions and formation of mono-ligand and multi-ligand complexes. The calculated log $K_{NPsCOOPb+}$ was 2.72, a value close to the log $K_{CH3COOPb^+} = 2.68$, as referenced in Martell and Smith (1989). Unfortunately, the constraint

imposed by the model calculation meant that it is not possible to discuss the log $K_{(CH3COO)2Pb}$ which depends on the log $K_{NPsCOOPb^+}$.

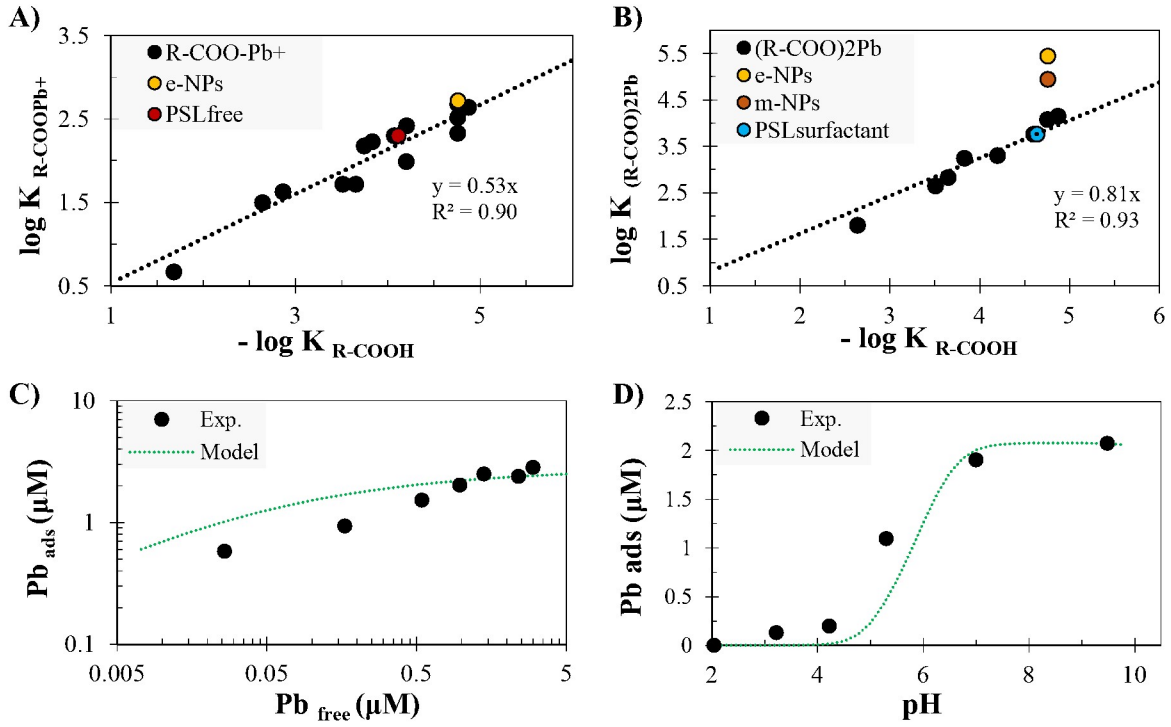

Fig. 5. Surface complexation model validation. A-B) LFER of log $K_{R\text{-}COOPb^+}$ and log $K_{(R\text{-}COO)_2Pb}$ relative to the dissociation constant of various carboxylic ligands, log $K_{R\text{-}COOH}$ (adapted from Carbonaro and Di Toro, 2007, and [35], and the studied NPs. **C-D)** Experimental (black points) and estimated (dotted lines) Pb(II) concentrations adsorbed onto e-NPs prepared by Davranche et al. (2019).

To further validate the calculated log K, were compared the log K of R-COO-Pb^+ and $(R\text{-}COO)_2Pb$ by using a linear free energy regression (LFER), in which R is the radical of the various mono carboxylate acids (Fig. 5 A and B). For the mono-ligand complex, the log K calculated for the e-NPs and PSL_{free} were situated in the highest values of the log K of $RCOOPb^+$ used for the LFER. However, the mechanistic model overestimated the value of the bi-ligand log K, especially for the m-NPs and e-NPs, for which the calculated log K was one order of magnitude higher than that for the LFER. This overestimation can be explained by the fixed values used for the model calculation (pKa, for the m-NPs and pKa, and both log K for the e-NPs).

The validity of the model was also tested with the datasets provided by Davranche et al. [12] (Fig. 5 C and D). Their e-NPs were produced using a similar protocol to the one described in Blancho et al.[19], but without natural organic matter (NOM) degradation. As the binding site density was unknown for

the e-NPs of Davranche et al. [12], this parameter was fitted. Modelling calculations determined a COOH total concentration of 0.114 mmol g^{-1}, in the same order of magnitude as the e-NPs produced here. The RMSE = 0.23 was slightly higher than for the other NPs but within the same order of magnitude. The model overestimated the bound Pb for the low Pb concentrations (from $[Pb]_{free} < 10^{-6}$ mol L^{-1}) and overestimated them for acidic pH (pH < 7) (Fig. 5 C and D). As previously explained, NOM was still present in the adsorption experiment carried out by Davranche et al. [12]. This NOM could have influenced the amount of Pb adsorbed by the NPs by complexing Pb and, competing with the NPs, forming aggregates (with and without NPs) at acidic pH. At acidic pH, dissolved OM could have aggregated to form bigger particles retained in the >3KDa fraction and thus bias the adsorbed Pb concentration. The formation of hetero-aggregates could also modify the binding site density of the NPs. However, at high Pb concentrations and pH (Fig. 5 C and D), it was possible to accurately predict $[Pb]_{ads}$, indicating no hetero-aggregation. Pradel et al.[37] demonstrated that the source of NOM was a significant parameter of the hetero-aggregation. They showed that hetero-aggregates could be formed with alginate but not with charged OM such as humic acid. These calculations show that the model needs to be improved, in particular to take into account the homo and hetero-aggregation that can occur in the presence of organic matter and at acidic pH. But the good reproducibility of the experimental datasets at circumneutral pH validated the binding hypothesis of our modelling approach.

Environmental implications

The model calculations suggested that mono and bi-ligand complexes are formed between Pb and NPs, except for PSL_{free}. For the e-NPs, both mono- and bi-ligand complexes are produced. Both parameters are controlled by the shape heterogeneity and the NPs aggregation (e.g. m-NPs). However, it seems as though the formed complex is controlled by the site density and the geometrical distribution of the $-COO^-$ sites. The present results highlight the role of the degree of NPs degradation which depends on the medium and the prevailing physicochemical conditions. In surface water (river and ocean), photooxidation is expected to be the primary process responsible for the alteration of the e-NPs. Photooxidation mainly produces COO^- binding sites, but their density will depend on the

View Article Online
DOI: 10.1039/D3EN00677H

residence time of the plastic debris in the ocean and river. In soil, the degradation is very low and occurs mainly through biotic processes [38], with UV penetrating only the very first cm of the uppermost layer of the soil. In this context, it is therefore expected that only a small amount of metal will be bound by e-NPs in the soil. By contrast, in compost made of household wastes and used for soil amendments, the composting process involves an intense alteration/oxidation of the plastics via the production of $OH^{\bullet}$ radicals able to produce COO^- sites [39]. In these conditions, NPs can act as metal adsorbents. Nonetheless, nanoparticles (NPs) can serve as effective adsorbents only when their concentration is sufficiently high to compete with other soil adsorbents, such as natural organic matter and Fe-oxyhydroxides. This is particularly applicable in soil lacking an organic horizon or in soils with low iron content. Furthermore, it is essential to take into account the influence of eco-corona formation[40], which can either modify the availability of NPs' adsorption sites or enhance metal adsorption by creating new binding sites (additive effect).

Aggregation also seems to impact the sorption process at the NPs surface. Intuitively, aggregation is considered a limitation to metal binding in response to the decreasing availability of sites. However, the results suggest that aggregation associated with the shape heterogeneity can favor metal adsorption by controlling the geometrical distribution of the functional group and creating a local high binding site density that favors the formation of multidentate complexes. Nevertheless, one consequence of this aggregation is the enlargement of particle size, leading to a subsequent reduction in the colloidal stability of the nanoparticles (NPs). As a result, while aggregation may facilitate the formation of a stable complex between the metal and NPs, it can also lead to the entrapment of NPs along with the bound metal within soil pores or sediment due to NPs settling.

Lead may also be present in the plastic matrices as additives. It is expected that lead will be released during the photooxidation of the polymer and then partly adsorbed on the altered layer of the MPs that will further be altered as NPs. Catrouillet et al.[21] calculated a median concentration of Pb in MPs close to 0.3 mg $Kg^{-1}C$, i.e. 6500 times lower than the Pb potentially adsorbed by the e-NPs. These authors suggested that the Pb adsorbed on the altered surface of MPs originated from Pb used as additives rather than from the environment. Although this adsorption by NPs partly prevents the

release of the metal, it could also favor their transfer during the colloidal phase in ecosystems and living organisms.

Conclusions

To the best of our knowledge, this work is the first to design a surface complexation model to describe and predict the adsorption of Pb by NPs. Following the previous study[12,20], two binding hypotheses were tested to explain the adsorption of Pb by NPs. For all NPs models, carboxyl complexes dominate lead adsorption, and bi-ligand adsorption occurred for the $PSL_{surfactant}$, m-NPs, and e-NPs models. The extrapolated log K was consistent with the log K RCOO-Pb and log K $(RCOO)_2Pb^+$ values from the literature, validating the NPs adsorption models (Fig.s 7 and 8). Metal-NPs interactions depend on the binding site density, shape and aggregation. Milled NPs are less reactive to metal than strongly NPs photo-oxidized under environmental conditions. These results also highlighted the influence of the NPs degradation pathway on the NPs shape and binding site density distribution and thus availability to form mono or bi-ligand complexes. Although NPs competition with natural adsorbents is expected to be low and dependent on their concentration, multi-component sorption should be better studied within environmental conditions to define the metals associated with NPs in the environment. Moreover, competition between metals must be studied in further detail to identify metals having the highest affinity for NPs. Such studies would include a mechanistic approach in order to complete the sorption models proposed in this study and to test their reliability in predicting metal sorption in a more complex matrix.

Conflicts of interest

There are no conflicts of interest to declare.

Source of financial support

The authors declare that they have no known competing financial interests or personal relationships that could have appeared to influence the work reported in this paper. This work was supported by

the ANR (Agence Nationale de la Recherche) PRC program through the PEPSEA (ANR-17-CE34-0008-05) and PLASTISCARE (ANR-19-CE04-0007) projects as well as the CNRS EC2CO-HYBIGE program via the NAME project. Through the support of the GeOHeLiS analytical platform at Rennes University, this publication is also supported by the European Union through the European Regional Development Fund (FEDER), the French Ministry of Higher Education and Research, the French Region of Brittany, and Rennes Metropole.

Acknowledgments

We also acknowledge Ludivine Rault for the TEM observations performed at THEMIS 476 (ScanMAT, UMS 2001 CNRS - University of Rennes 1). Dr. Sara Mullin is also acknowledged for proofreading the English content (https://fr.linkedin.com/in/sara-mullin-0b53b112/fr). We would also like to thank Mrs. Fatimah Sulu Gambari and Laurent Lebreton from Ocean Cleanup for providing the altered plastic debris necessary to produce the e-NPs.

References

1 A. Ter Halle, L. Jeanneau, M. Martignac, E. Jardé, B. Pedrono, L. Brach and J. Gigault, *Environmental Science & Technology*, 2017, **51**, 13689–13697.

2 D. Materić, A. Kasper-Giebl, D. Kau, M. Anten, M. Greilinger, E. Ludewig, E. van Sebille, T. Röckmann and R. Holzinger, *Environ. Sci. Technol.*, 2020, **54**, 2353–2359.

3 A. Wahl, C. Le Juge, M. Davranche, H. El Hadri, B. Grassl, S. Reynaud and J. Gigault, *Chemosphere*, 2021, **262**, 127784.

4 J. Gigault, H. El Hadri, B. Nguyen, B. Grassl, L. Rowenczyk, N. Tufenkji, S. Feng and M. Wiesner, *Nat. Nanotechnol.*, 2021, **16**, 501–507.

5 J. Gigault, A. ter Halle, M. Baudrimont, P.-Y. Pascal, F. Gauffre, T.-L. Phi, H. El Hadri, B. Grassl and S. Reynaud, *Environmental Pollution*, 2018, **235**, 1030–1034.

6 D. Brennecke, B. Duarte, F. Paiva, I. Caçador and J. Canning-Clode, *Estuarine, Coastal and Shelf Science*, 2016, **178**, 189–195.

7 D. Brennecke, B. Duarte, F. Paiva, I. Caçador and J. Canning-Clode, *Estuarine, Coastal and Shelf Science*, 2016, **178**, 189–195.

8 A. Turner, L. A. Holmes, A. Turner and L. A. Holmes, *Environ. Chem.*, 2015, **12**, 600–610.

9 S. Tang, L. Lin, X. Wang, A. Yu and X. Sun, *Journal of Hazardous Materials*, 2021, **403**, 123548.

10 X. Guo and J. Wang, *Journal of Hazardous Materials*, 2021, **402**, 123709.

11 E. Besseling, P. Redondo-Hasselerharm, E. M. Foekema and A. A. Koelmans, *Critical Reviews in Environmental Science and Technology*, 2019, **49**, 32–80.

12 M. Davranche, C. Veclin, A.-C. Pierson-Wickmann, H. El Hadri, B. Grassl, L. Rowenczyk, A. Dia, A. Ter Halle, F. Blancho, S. Reynaud and J. Gigault, *Environmental Pollution*, 2019, **249**, 940–948.

13 Q. Chen, D. Yin, Y. Jia, S. Schiwy, J. Legradi, S. Yang and H. Hollert, *Science of The Total Environment*, 2017, **609**, 1312–1321.

14 X. Jiang, L. Tian, Y. Ma and R. Ji, *Science of The Total Environment*, 2019, **655**, 591–597.

15 L. Pessoni, C. Veclin, H. El Hadri, C. Cugnet, M. Davranche, A.-C. Pierson-Wickmann, J. Gigault, B. Grassl

View Article Online
DOI: 10.1039/D3EN00677H

and S. Reynaud, *Environ. Sci.: Nano*, 2019, **6**, 2253–2258.

16 D. M. Mitrano, A. Beltzung, S. Frehland, M. Schmiedgruber, A. Cingolani and F. Schmidt, *Nature Nanotechnology*, 2019, **14**, 362–368.

17 D. Magrì, P. Sánchez-Moreno, G. Caputo, F. Gatto, M. Veronesi, G. Bardi, T. Catelani, D. Guarnieri, A. Athanassiou, P. P. Pompa and D. Fragouli, *ACS Nano*, 2018, **12**, 7690–7700.

18 H. El Hadri, J. Gigault, B. Maxit, B. Grassl and S. Reynaud, *NanoImpact*, 2020, **17**, 100206.

19 F. Blancho, M. Davranche, F.-S. Fumagalli, G. Ceccone and J. Gigault, *Environ. Sci.: Nano*, 2021, 10.1039.D1EN00395J.

20 F. Blancho, M. Davranche, R. Marsac, A. Léon, A. Dia, B. Grassl, S. Reynaud and J. Gigault, *Environmental Science: Nano*, , DOI:10.1039/D2EN00048B.

21 C. Catrouillet, M. Davranche, I. Khatib, C. Fauny, A. Wahl and J. Gigault, *Environ. Sci.: Processes Impacts*, 2021, **23**, 553–558.

22 H. El Hadri, J. Gigault, B. Maxit, B. Grassl and S. Reynaud, *NanoImpact*, 2020, **17**, 100206.

23 ISO 9277, https://www.iso.org/fr/standard/71014.html, (accessed January 3, 2024).

24 L. Spadini, A. Navel, J. M. F. Martins, E. Vince and I. Lamy, *European Journal of Soil Science*, 2018, **69**, 953–961.

25 D. L. Parkhurst and C. A. J. Appelo, *User's guide to PHREEQC (Version 2): A computer program for speciation, batch-reaction, one-dimensional transport, and inverse geochemical calculations*, 1999.

26 D. Kinniburgh and D. Cooper, *PhreePlot: Creating graphical output with PHREEQC*, 2011.

27 M. J. D. Powell, *The Computer Journal*, 1965, **7**, 303–307.

28 C. Pfeiffer, C. Rehbock, D. Hühn, C. Carrillo-Carrion, D. J. de Aberasturi, V. Merk, S. Barcikowski and W. J. Parak, *J. R. Soc. Interface.*, 2014, **11**, 20130931.

29 K. A. Connors, *Chemical kinetics: the study of reaction rates in solution*, VCH, New York, N.Y, 1990.

30 J. Chen, J. Hu, Y. Xu, R. Krasny and W. Geng, *J. Comput. Biophys. Chem.*, 2021, **20**, 175–187.

31 A. E. Martell and R. M. Smith, *Other Organic Ligands*, Springer US, Boston, MA, 1977.

32 J. Lützenkirchen, J. van Male, F. Leermakers and S. Sjöberg, *J. Chem. Eng. Data*, 2011, **56**, 1602–1612.

33 M. Tesfa, J. F. L. Duval, R. Marsac, A. Dia and J.-P. Pinheiro, *Environ. Sci. Technol.*, 2022, **56**, 10494–10503.

34 P. Hesleitner, D. Babic, N. Kallay and E. Matijevic, *Langmuir*, 1987, **3**, 815–820.

35 R. M. Smith and A. E. Martell, in *Critical Stability Constants: Second Supplement*, eds. R. M. Smith and A. E. Martell, Springer US, Boston, MA, 1989, pp. 299–359.

36 R. F. Carbonaro and D. M. Di Toro, *Geochimica et Cosmochimica Acta*, 2007, **71**, 3958–3968.

37 A. Pradel, S. Ferreres, C. Veclin, H. El Hadri, M. Gautier, B. Grassl and J. Gigault, *ACS EST Water*, 2021, **1**, 1198–1208.

38 Y. Otake, T. Kobayashi, H. Asabe, N. Murakami and K. Ono, Biodegradation of low-density polyethylene, polystyrene, polyvinyl chloride, and urea formaldehyde resin buried under soil for over 32 years - Otake - 1995 - Journal of Applied Polymer Science - Wiley Online Library, https://onlinelibrary.wiley.com/doi/abs/10.1002/app.1995.070561309?casa_token=zdLRdpw_HpEAAAAA:FW_O4L_aD76t4Y-2DDUFrVry-6LX7nghsKv6FVtegOVJayJh4PnhdIPoE6ipQzZlgF5Z_GBoqbwCtpY, (accessed July 19, 2022).

39 R. Xing, Z. Chen, H. Sun, H. Liao, S. Qin, W. Liu, Y. Zhang, Z. Chen and S. Zhou, *Journal of Hazardous Materials*, 2022, **429**, 128405.

40 M. Junaid and J. Wang, *Water Research*, 2021, **201**, 117319.